Investigations of discharge and post-discharge in a gliding arc : a 3D computational study

Investigations of discharge and post-discharge in a gliding arc: a 3D computational study

SR Sun[1,2], St Kolev[3], HX Wang[1] and A Bogaerts[2]

[1] School of Astronautics, Beihang University, 100191, Beijing, China
[2] Research group PLASMANT, Department of Chemistry, University of Antwerp, Universiteitsplein 1, B-2610, Antwerp, Belgium
[3] Faculty of Physics, Sofia University, 5 James Bourchier Boulevard, 1164 Sofia, Bulgaria

E-mail: annemie.bogaerts@uantwerpen.be , whx@buaa.edu.cn

Abstract. In this study we quantitatively investigate for the first time the plasma characteristics of an argon gliding arc with a 3D model. The model is validated by comparison with available experimental data from literature and a reasonable agreement is obtained for the calculated gas temperature and electron density. A complete arc cycle is modeled from initial ignition to arc decay. We investigate how the plasma characteristics, i.e., the electron temperature, gas temperature, reduced electric field, and the densities of electrons, Ar^+ and Ar_2^+ ions and Ar(4s) excited states, vary over one complete arc cycle, including their behavior in the discharge and post-discharge. These plasma characteristics exhibit a different evolution over one arc cycle, indicating that either the active discharge stage or the post-discharge stage can be beneficial for certain applications.

Keywords: gliding arc, 3D model, arc cycle, post-discharge

1. Introduction

The gliding arc discharge has been attracting great interest in recent years due to its non-equilibrium property and its ability to produce a high density of charged particles and active species, which is important for a wide range of industrial applications [1-4]. The gliding arc is generated between a pair of flat electrodes, connected to a power source and submerged in a laminar or turbulent gas flow. The arc is ignited at the shortest interelectrode gap when the electric field is high enough to cause breakdown. The arc expands upwards along the surface of the electrodes upon effect of the gas flow, and elongates until it extinguishes. Subsequently, a new arc is initiated at the narrowest gap, and the process is repeated [5-7].

The gliding arc discharge allows the use of high power, which leads to the formation of a large amount of active species. Although initially developed for gas treatment [8], it can easily be adapted for surface [9] and even liquid treatments [10-13]. The first liquid targets tested were chemical pollutants (industrial waste, organic components and solvents) present in water [10-13]. However, plasma generated by a gliding arc discharge also shows potential for bacterial decontamination of liquids [14]. Although the active plasma stage of the gliding arc has been mostly used in industrial applications, some experiments have revealed that the post-discharge is also very promising, because the effect of the plasma can continue when the discharge is switched off, and therefore without consuming further energy [15, 16].

The gliding arc has been widely used for gas treatment due to its simultaneously high productivity and good selectivity [17]. The reasonably high electron energy and charged particle density in the active arc (with considerable current density) have a major effect on the treated gas, due to the high current density and Joule heating. However, some excited species have a relatively long lifetime and considerable internal energy, so they can still be active even during the post-discharge stage. Therefore, in some applications, such as the treatment of liquid and sensitive surfaces [18], the gliding arc could be predominantly used as a source of post-discharge plasma. Obviously, in this case we need to know how long is the lifetime of the excited species, which have enough energy to modify the surface. In order to better control the use of either discharge or post-discharge phase for industrial applications, it is indispensable to investigate the plasma characteristics in both the discharge and post-discharge of a gliding arc. Therefore, in this work we present the properties of both the active arc, with considerable current density, and the post-discharge plasma, with practically zero current and lower densities of active species, by means of computer modeling.

Although 2D modeling of a GA discharge has been reported, it can only qualitatively explain the phenomena occurring in the GA discharge, for example, the arc root movement, the back-breakdown phenomenon, etc [19-21]. In [21], we demonstrated that the 2D modeling approach is reasonable and useful to investigate the gliding arc behavior, by comparing with 3D modeling results, based on certain assumptions about gas flow and electric current in the 2D model. However, if we want to fully capture the gas flow effects and electric current, a 3D model is indispensable. In fact, the plasma characteristics of the gliding arc can only be described quantitatively in a 3D model, because the gas flow and arc column size really require a 3D model, using the real geometry. However, 3D modeling of a (gliding) arc remains scarce due to the long computation time. To date, the published 3D models in literature are based on local thermodynamic equilibrium [22-26] or on the two-temperature thermal non-equilibrium and chemical equilibrium assumption [27]. In [28] a thermal non-equilibrium and chemical non-equilibrium 3D model was employed to describe a reverse vortex flow gliding arc reactor, but the number of chemical reactions was limited. In our paper, a 3D model is developed without these simplifications, but this is at the expense of the computational cost. Nevertheless, we present here the evolution of the plasma characteristics in a gliding arc discharge, calculated with a 3D model over one complete arc cycle.

In our paper, we also investigate for the first time the effect of turbulent gas flow on the plasma characteristics of a gliding arc discharge. It is indeed reported from experiments [29] that a comprehensive numerical model, including the turbulent convection and plasma chemistry, is required to provide quantitative understanding of a gliding arc discharge. However, the approach of Direct Numerical Simulation (DNS), which is mostly associated with modeling of turbulent flows, aims to solve all scales of the flow, hence using extremely fine meshes, and extremely small time steps. Thus, computing turbulent gas flows in 3D requires very high computational power, as it requires solving the Navier-Stokes equations in a much finer mesh than required for laminar flow. For this reason, we simulate here the gas flow using the so-called k-ω Reynolds-averaged-Navier-Stokes (RANS) turbulent modeling technique, which effectively averages all fluctuating turbulent quantities over time, greatly

reducing the computational cost.

In section 2 we present our model, which uses the quasi-neutrality assumption and a reduced chemistry set and number of species. These assumptions are necessary in order to run the 3D model within a reasonable computation time. Moreover, we have validated the quasi-neutrality assumption by comparison with a non-quasi-neutrality model in [30]. In the results and discussion part we first compare our calculation results with experimentally measured data, in order to validate the 3D model. After this validation, we investigate the arc ignition, propagation and decay phenomena, i.e., the evolution of the plasma characteristics over one complete arc cycle. Finally, the conclusions will be given in section 4.

2. Description of the model

2.1 *Gliding arc geometry*

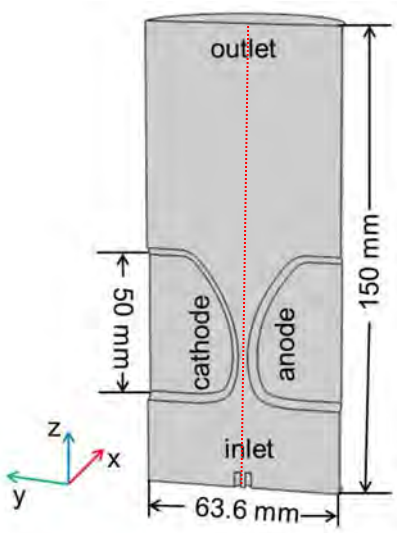

Figure 1. 3D Cartesian geometry used in the model. The zero of the z-axis in the figures below is at the position of the shortest interelectrode gap, which is 43 mm from the position of the gas nozzle (gas inlet).

The 3D Cartesian geometry used in our model is presented in figure 1. It is based on the gliding arc reactor studied by Tu and colleagues [31, 32], for which experimental data are available to validate our model. Figure 1 shows a cross section through the middle of the anode and the cathode, i.e., the cathode and anode in reality have a width of 5 mm, but only half of it is considered here. The shortest interelectrode distance is 3.2 mm in the model, which is the same as in the experiments [31, 32]. The entire model geometry, including the region outside the electrodes where the gas can flow without passing through the arc, is a cylinder, with radius of 31.8 mm. Besides the symmetry plane through the middle of the anode and cathode, as shown in figure 1, we also assume another symmetry plane between the anode and cathode in the 3D model, indicated by the red thin dashed line in figure 1. This allows us to model 1/4 of the total domain. The latter significantly reduces the calculation time.

2.2 *System of equations*

The plasma discharge equations are the same as in our previous paper [21]. They describe the plasma density, electron and gas temperature, and the electric field in the gliding arc. However, the gas flow description is now different from our previous paper [21], because we use here the k-ω Reynolds-averaged-Navier-Stokes (RANS) turbulent model. The following Navier-Stokes equations for Newtonian fluid are solved for the gas flow:

$$\vec{\nabla}\cdot(\rho\vec{u}_g)=0 \tag{1}$$

$$\rho(\vec{u}_g\cdot\vec{\nabla})\vec{u}_g=\vec{\nabla}\cdot(-p_g\hat{I}+(\mu+\mu_T)(\vec{\nabla}\vec{u}_g+(\vec{\nabla}\vec{u}_g)^T)-\frac{2}{3}(\mu+\mu_T)(\vec{\nabla}\cdot\vec{u}_g)\hat{I}-\frac{2}{3}\rho k\hat{I}) \tag{2}$$

$$\rho(\vec{u}_g\cdot\vec{\nabla})k=\vec{\nabla}\cdot[(\mu+\mu_T\sigma_k^*)\vec{\nabla}k]+P_k-\beta_0^*\rho\omega k \tag{3}$$

$$\rho(\vec{u}_g\cdot\vec{\nabla})\omega=\vec{\nabla}\cdot[(\mu+\mu_T\sigma_\omega)\vec{\nabla}\omega]+\alpha\frac{\omega}{k}P_k-\rho\beta_0\omega^2 \tag{4}$$

$$P_k=\mu_T[\vec{\nabla}\vec{u}_g:(\vec{\nabla}\vec{u}_g+(\vec{\nabla}\vec{u}_g)^T)-\frac{2}{3}(\vec{\nabla}\cdot\vec{u}_g)^2]-\frac{2}{3}\rho k\vec{\nabla}\cdot\vec{u}_g \tag{5}$$

where ρ is the gas density, u_g is the gas flow velocity, p_g is the pressure, μ is the dynamic viscosity and μ_T is the turbulent viscosity of the fluid, k is the turbulent kinetic energy, $\hat{I}$ is the identity matrix and the superscript 'T' stands for the tensor transpose operation. ω is the turbulent dissipation rate, P_k is the production of kinetic energy k, and σ_k^*, σ_ω, β_0^*, β_0 and α are turbulence model parameters (see [33] for more details). In our case, the RANS equations are not solved together with the other equations, because this would lead to excessive calculation times. Instead, the RANS equations are first solved separately in order to provide a solution for a fully developed gas flow, which is subsequently used as initial condition for the system of plasma discharge equations. Then the other plasma equations are solved simultaneously using the obtained velocity as input data, i.e., the equations for the electric potential, species densities, gas temperature and electron energy are solved in a coupled way.

We apply a reduced chemistry set in order to calculate the 3D model within a reasonable time. We consider five important species, i.e., Ar, Ar(4s), Ar^+, Ar_2^+ and the electrons (*e*), and their chemical reactions are the same as the corresponding reactions listed in table 1 in [21]. In our case, the calculated radiation energy loss using the formula in literature [34-36] is relatively minor compared with the elastic collision energy loss and inelastic collision energy loss caused by chemical reactions, so we neglect its effect in the calculations.

The arc is first ignited in the model by using a time and space dependent heat source term that creates a conducting plasma channel between the cathode and the anode wall. At the beginning, the gas electrical conductivity is very low, so when adding this artificial heating term to initiate the discharge, the gas resistance decreases in a short time, thus leading to a sharp voltage drop. Then the voltage drops further until a stable self-sustained plasma channel is formed, i.e., the discharge is ignited at the shortest interelectrode distance. After this, the

arc voltage increases under the effect of the gas flow, so the next ignition of the arc at the shortest interelectrode gap is caused by the large arc voltage.

The boundary conditions to solve the plasma discharge equations, i.e., for the plasma density, electron energy, heat transfer and electric potential equation, are the same as defined in [21]. The anode electric potential is zero (anode connected to ground). The cathode potential is derived from Ohm's law based on the total cathode current and the external circuit. For the species density and electron energy equations, zero species fluxes and zero electron energy flux are set at the walls, and a zero gradient of the species density and the electron energy density are set at the inlet and the outlet. The thermal insulation boundary condition is used on the electrode walls, the temperature is fixed at 293.15 K at the inlet, while a zero temperature gradient is assumed at the outlet. For the inlet condition of gas flow, here we define the normal inflow velocity at the nozzle inlet, which has a small diameter of 1.5 mm, to obtain a gas flow rate of 10 L/min.

3. Results and discussion

3.1 *Validation of the model: Comparison between calculated and experimental values*

In order to validate our 3D model, we plot in figure 2(a) the maximum value of the calculated gas temperature along the z-axis at different times , together with the experimental values, obtained from [31] at a current of 28 mA and a gas flow rate of 10 L/min. The results are plotted as a function of the distance of the maximum T_g value from the shortest interelectrode gap - the arc moves in time and thus the maximum value appears at different distances. The z-axis on which the results of figure 2(a) are sampled, is marked with a white dashed line in figure 2(b), which illustrates the 2D distribution of the gas temperature in the yz plane at a time of 0.2 ms. The calculated gas temperature first increases rapidly from 300 K to 570 K, and afterwards, it increases slightly upon larger axial distance. The first increase of the gas temperature is caused by the arc ignition, due to the energy exchange in collisions between electrons and heavy particles. After the ignition, the gas temperature increases only slightly, which can be explained by the slightly decreasing gas heating source term and the strong convective and conductive cooling loss terms in the 3D model. As will be shown in section 3.2, within one arc cycle, the electron temperature almost stays constant at 2.6 eV, and the electron density gradually decreases with time. So the elastic energy transfer from the electrons to the heavy particles slightly decreases, which results in a slight decrease of gas heating with time. Moreover, the convective and conductive cooling prevent further arc contraction, and thus the gas temperature rise is limited. Hence, the combination of the gas heating source term (i.e., slightly decreasing) and the cooling loss term results in only a minor increase of the gas temperature with axial distance after ignition of the arc.

The maximum experimental gas temperature reported in [31] is about 500 K, which is about 30% lower than our maximum calculated gas temperature of about 650 K. This difference can be explained by some experimental factors, which are not considered in the simulations, like the phenomenon of back-breakdown and the arc jump attachment on the surface of the cathode. Indeed, these phenomena both result in a slower arc velocity than the gas flow

velocity, and this causes a lower gas temperature inside the arc [19, 21]. Due to the complexity of the model, these factors are not considered in the present 3D model, because this would lead to excessive computation times. Indeed, the calculation time of the present 3D model is about 12 days for one complete arc cycle through the GA reactor, and in previous work of our group [30], we found that taking into account the arc jump attachment on the surface of the cathode, in a 2D model, causes an increase of the calculation time by a factor 5. Thus it is clear that taking this effect into account would indeed yield too long calculation times in a 3D model.

We would like to note that our earlier simulations in 2D predicted much higher values of the maximum gas temperature, i.e., in the order of about 1200 K [19, 21]. The reason why our new model already yields better agreement with the experimental gas temperature is because the turbulent convective cooling is considered in this model. Hence, it is clear that our 3D model presented here can provide a much more realistic picture for the gas temperature.

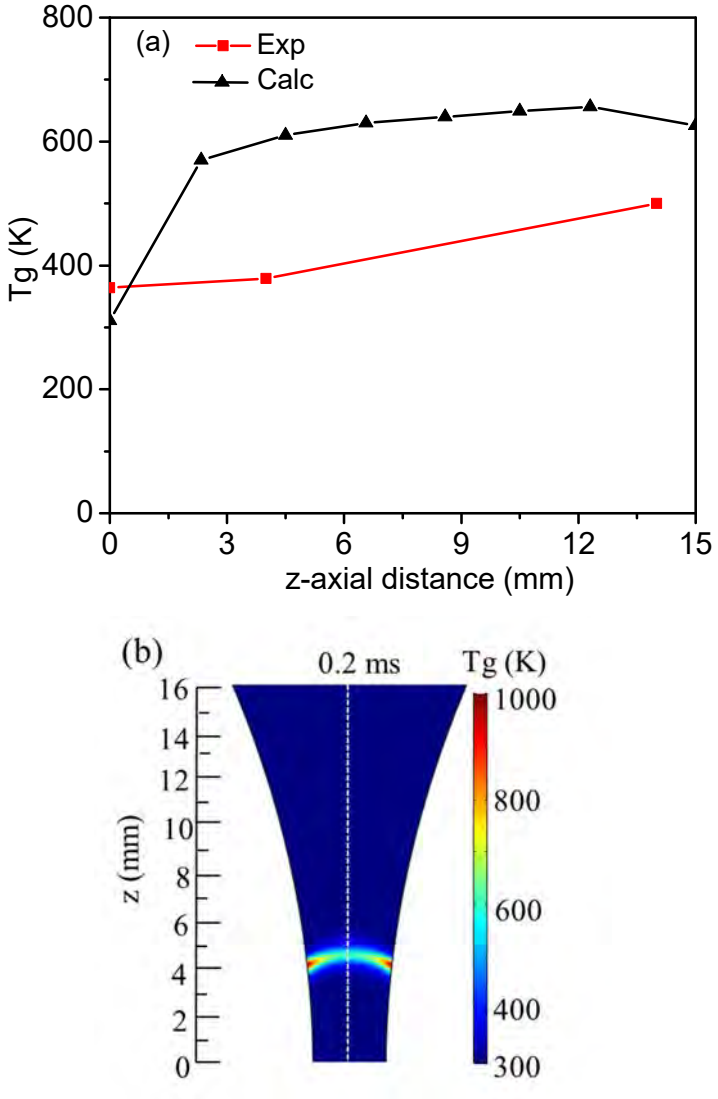

Figure 2. (a) Comparison of calculated maximum gas temperature along the z axis with experimental values obtained from [31], as a function of z-axial distance from the shortest interelectrode gap. The z-axial distance corresponds to different times of the arc evolution

(the last position of 15 mm corresponds to a time of 0.7 ms). (b) is an illustration of the gas temperature distribution in the yz plane at t=0.2 ms , for a current of 28 mA and a gas flow rate of 10 L/min.

Figure 3(a) shows the maximum value of the electron density along the z axis (in the arc center), at different times corresponding to different z-axial positions. The electron density distribution in the yz plane is presented in figure 3(b) at t=0.2 ms, in which the z-axis is marked with a white dashed line. It is clear from figure 3(a) that after ignition of the arc, the electron density slightly drops with increasing z-axial position, from 6×10^{20} to 3×10^{20} m^{-3}. In [31] an electron density in the order of 5×10^{22} m^{-3} was measured for an argon gliding arc, so these values are two orders of magnitude higher than our calculated values. However, we believe that these measured values are too high, because they correspond to conditions close to an LTE plasma at 1 atm [37, 38], and we clearly show that the gliding arc under study is far from LTE. The gas temperature measurements in [31] also clearly state that the plasma is far from LTE. Furthermore, in [39] the electron density was measured to be about 5×10^{21} m^{-3} for an argon gliding arc at a current of about 200 mA. This is about one order of magnitude higher than our calculated values, but the current was also one order of magnitude higher, and we expect the current to be linearly proportional to the electron density. Furthermore, in [40], an electron density in the order of 9×10^{19} m^{-3} was reported for an argon gliding arc, at a current density of about 10^5 A/m^2, which is similar to our calculated current density (i.e., about 3×10^5 A/m^2). Therefore, we believe that our calculated electron density is within a realistic range.

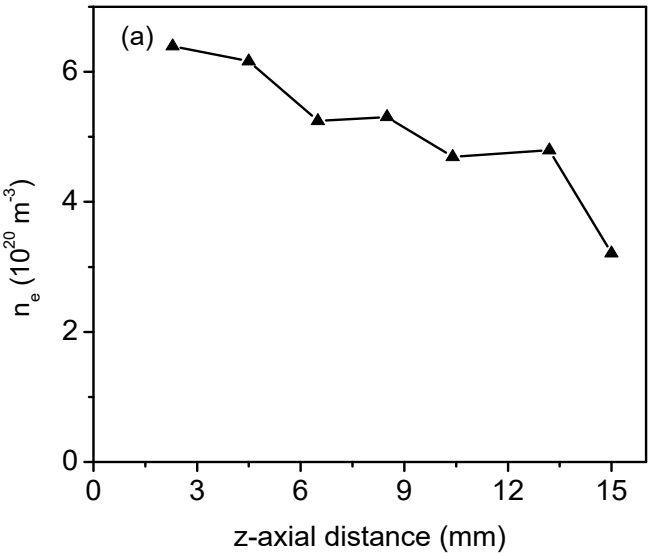

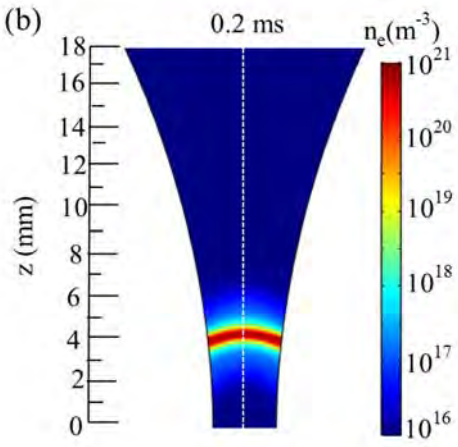

Figure 3. Calculated maximum electron density (in the center of the arc) along the z axis, as a function of distance from the shortest interelectrode gap (a), and illustration of the electron density distribution in the yz plane (b), for a current of 28 mA and a gas flow rate of 10 L/min.

3.2 *Evolution of plasma characteristics in discharge and post-discharge*

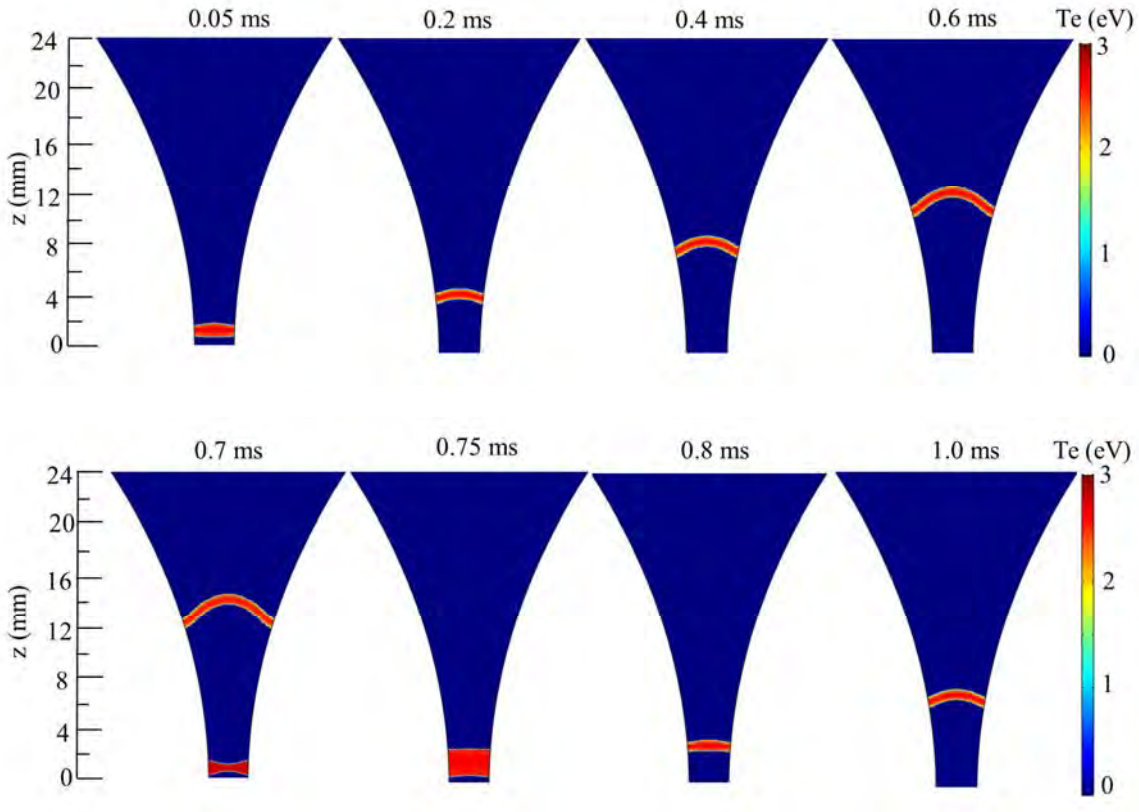

Figure 4. Time and spatial evolution of the electron temperature in the yz plane, at a current of 28 mA and a gas flow rate of 10 L/min.

Figure 4 presents the time and spatial evolution of the electron temperature in the yz plane at a current of 28 mA and a gas flow rate of 10 L/min. The electron temperature in the arc center (core) almost stays constant at 2.6 eV within one arc cycle. At a time of about 0.7 ms, a new arc is formed at the shortest interelectrode gap, with a somewhat larger electron temperature

of 2.76 eV, which is caused by the larger electric field, as shown in figure 5 below. This higher electron temperature results in more electrons produced at the shortest gap, as will be shown below. As a result of this, a new arc forms at the shortest interelectrode gap, the old arc disappears, and the arc cycle repeats itself. When the old arc begins to disappear, the electron temperature almost immediately (i.e., within a time shorter than 50 μs) drops to a value similar to the background plasma, which means that the electric field also drops to values corresponding to the background plasma, as shown in figure 5 below.

The reduced electric field (E/N) is a very important parameter for non-equilibrium plasmas, as it determines whether the plasma is in equilibrium or not. Only at very low E/N values (<< 1 Td or 10^{-21} V·m^2), the electron energy comes close to the kinetic energy of the heavy particles [41]. As seen in Figure 5, at a time of 0.05 ms, there is a strong reduced electric field of 2.96×10^{-21} V·m^2, resulting in the initiation of a new arc. After the ignition of the arc, the evolution of the reduced electric field is similar to that of the electron temperature, i.e., it slightly decreases from 2.8×10^{-21} to 2.6×10^{-21} V·m^2 (or from 2.8 to 2.6 Td). This reduced electric field is sufficient for ionization, and for sustaining the arc operation. In [42], a reduced electric field value of 6 Td was reported for a gliding arc discharge in air, based on measured values of the electric field strength. Hence, this is in the same order of magnitude as our calculated values. Because oxygen is an electronegative gas, electron attachment can compete with electron production by ionization. Therefore, a somewhat higher electric field is needed to sustain the arc in air than in argon.

It is thus clear that the reduced electric field needed to sustain the arc during the discharge stage is relatively high, demonstrating that the gliding arc is non-thermal, but in the post-discharge stage, the reduced electric field quickly drops to the background value, as shown at a time of 0.75 ms in figure 5. At the time of 0.8 ms, a strong reduced electric field of 2.96×10^{-21} V·m^2 again occurs at the shortest gap, which is similar to the value at the time of 0.05 ms, resulting in a new arc cycle.

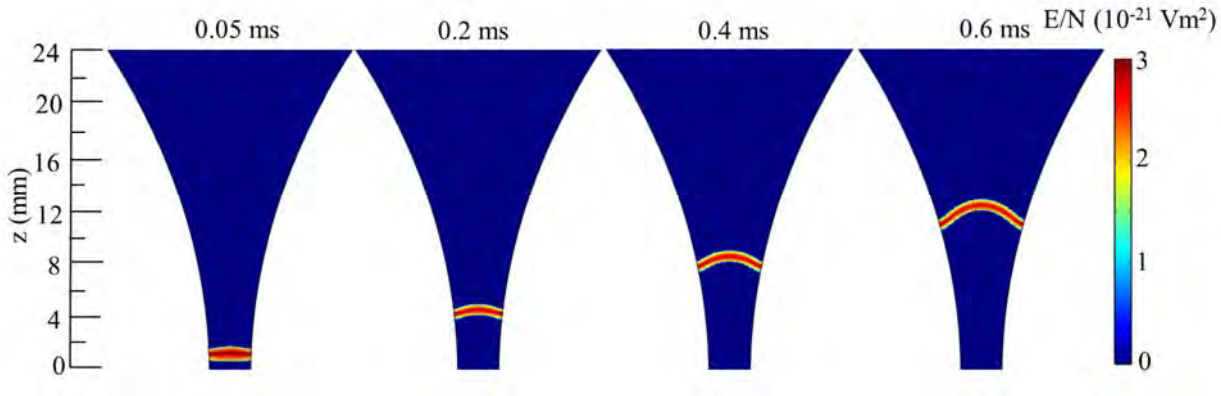

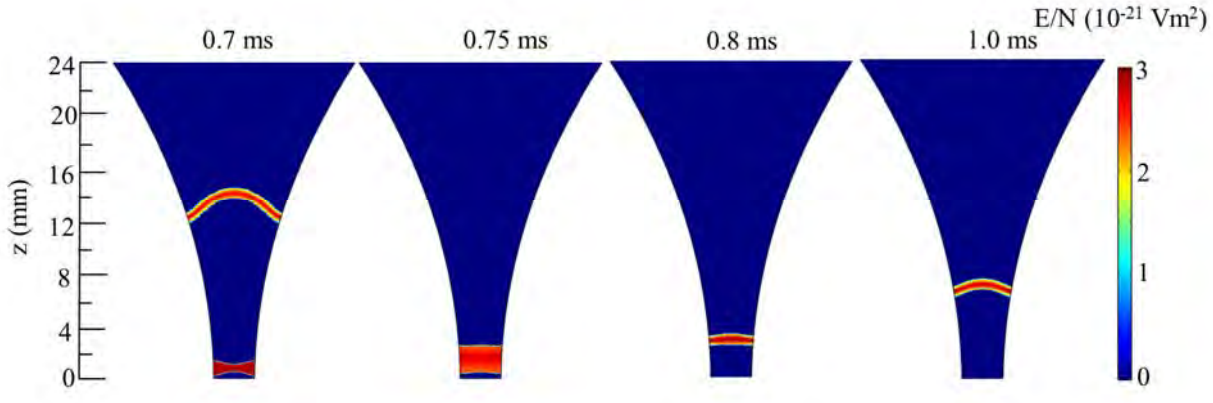

Figure 5. Time and spatial evolution of the reduced electric field in the yz plane, at a current of 28 mA and a gas flow rate of 10 L/min.

Note that the repetition cycle of the gliding arc, and thus the moment of appearance of a second arc at the shortest gap, is not exact and does not correspond to an actual experiment. In reality the breakdown at the shortest gap will appear at much higher electric field (or voltage between the electrodes) due to the considerable breakdown voltage of the argon gas. In the model the breakdown appears earlier since we impose a low density background plasma for improved model stability. This allows easier and thus earlier breakdown (i.e., at much lower breakdown voltage) and thus the period of cycle repetition is shorter than in reality, where it is around 8.4 ms for the conditions under study [31]. However, despite the early appearance of a secondary arc, the properties of the arc plasma and post-discharge plasma are expected to be realistic and unaffected by the repetition period.

The time and spatial evolution of the gas temperature in the yz plane is presented in figure 6, while figure 7 shows the 1D distribution of the gas temperature along the z-axis at different times.

At the time of 0.05 ms, the gas temperature is very low, i.e., 440 K at the center, which can be clearly seen from figure 7, while at this moment, the electron temperature and reduced electric field are already very high (see figure 4 and 5), causing ignition of the arc. From 0.05 ms to 0.2 ms, the gas temperature increases significantly, while it increases only slightly from 0.2 to 0.7 ms; this behavior was explained in section 3.1. At the time of 0.7 ms, when a new arc starts to ignite, as observed from the electron temperature and reduced electric field distributions in figures 4 and 5 above, the gas temperature is still very low at the position of the shortest gap, indicating that there is still only one arc in the entire region. Therefore, there is only one peak value of the gas temperature at this time in figure 7. However, both the electron temperature and reduced electric field have a maximum at the shortest gap at this time, indicating the ignition moment of the new arc.

In the post-discharge stage, after 0.7 ms, the gas temperature gradually decays, while the electron temperature and reduced electric field suddenly drop to the background values (see figure 4 and 5). In figure 7, two peaks are observed in the gas temperature profile from 0.75 to 1 ms. At the time of 0.75 ms, the gas temperature in the new developing arc (350 K) is still lower than the gas temperature in the afterglow of the previous arc (450 K), so the new arc

cannot be clearly seen yet from the 2D distribution at this moment, until the time of 0.8 ms, when the gas temperature in the new arc is 490 K, and the gas temperature in the post-discharge decreases to about 400 K. Due to the lower gas temperature in the post-discharge stage, the post-discharge can be used for surface treatment or cleaning without corrosion and melting [43], especially when dealing with heat-sensitive materials. From the great difference between the electron and gas temperature, at the conditions investigated here, it is clear that the gliding arc is a non-equilibrium plasma.

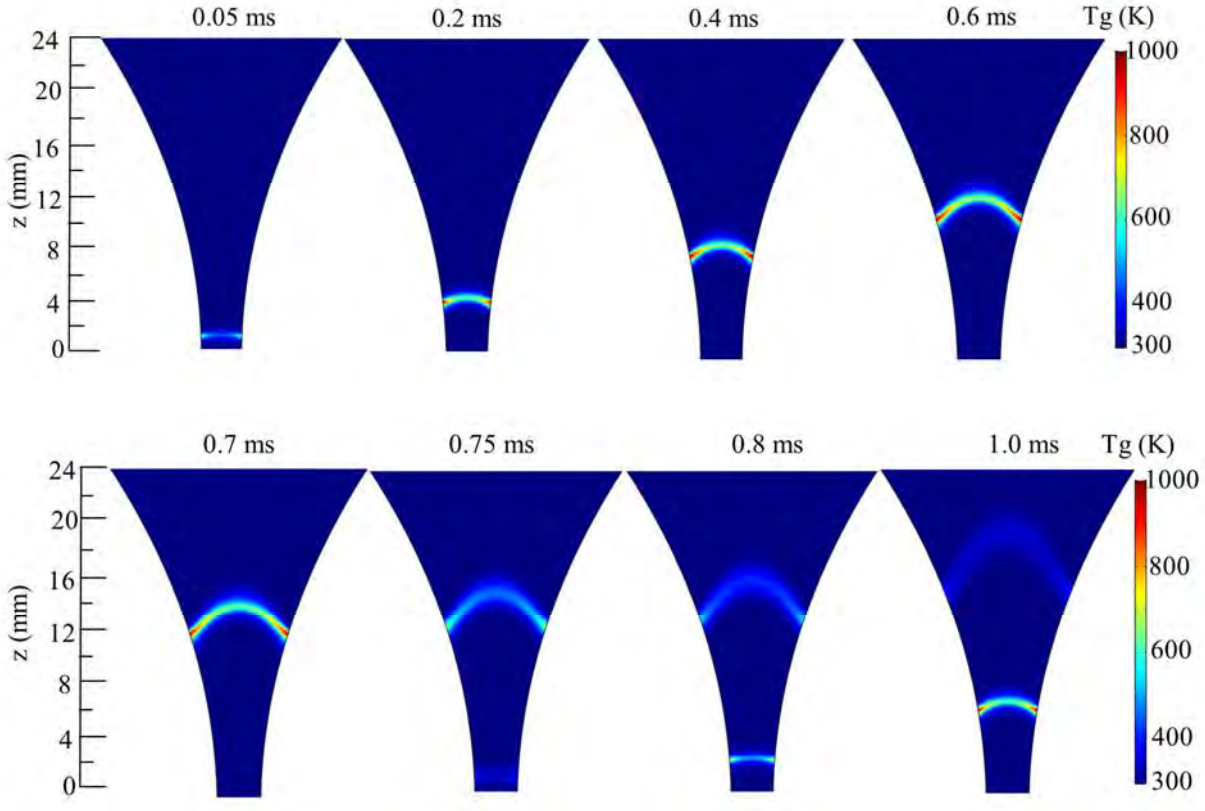

Figure 6. Time and spatial evolution of the gas temperature in the yz plane, at a current of 28 mA and a gas flow rate of 10 L/min.

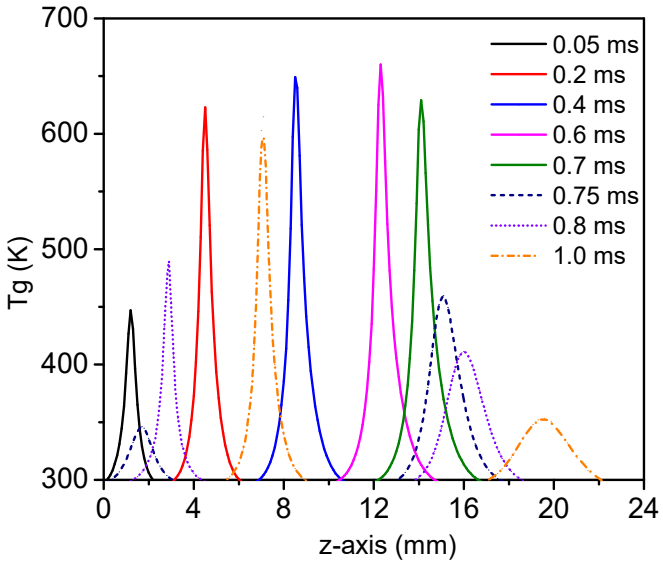

Figure 7. Distribution of gas temperature along the z-axis at different times, for a current of 28 mA and a gas flow rate of 10 L/min.

Figure 8 exhibits the time and spatial evolution of the electron density in the yz plane, at a current of 28 mA and a gas flow rate of 10 L/min, while figure 9 shows the 1D electron density distribution along the z-axis at different times.

At the time of 0.05 ms, the plasma discharge is ignited, and the arc glides along the electrodes under the influence of the gas flow. In the arc discharge stage, the electron density slightly drops with increasing z-axial position, from 6×10^{20} to 3×10^{20} m^{-3}, as also shown in figure 3(a) above. At the time of 0.7 ms, the larger electron temperature at the shortest interelectrode distance (see figure 4 above) results in a rise of the electron density at this position (see figure 8), i.e., to a value in the order of 6×10^{18} m^{-3}. Hence we can observe two peak values in figure 9 at 0.7 ms. The first peak value is lower, corresponding to the density at the shortest gap, while the second peak value is higher, corresponding to the old arc. This indicates the beginning of a new arc cycle, as explained above.

Although the electron density has a high value during the discharge stage, when the old arc begins to disappear, the electron density suddenly drops to a very low value of 6×10^{17} m^{-3} at a time of 0.75 ms (see figure 8 and 9). Hence, we only see a shade moving downstream during the post-discharge stage in the 2D distribution. Here we should note that despite the large drop in the peak density value, i.e., a factor 1500 between 0.7 ms and 0.8 ms, the total number of electrons actually decreases only by a factor 30 within this time interval. This is due to a spread of the plasma species in a wider channel.

Figure 10 presents the distribution of the Ar^+ and Ar_2^+ ion densities along the z-axis at different times, for a current of 28 mA and a gas flow rate of 10 L/min. During the active arc phase, the Ar^+ ions are dominant, with peak values up to a factor 10 higher than for the Ar_2^+ ions (see figure 10), while in the post-discharge stage, the Ar^+ ions suddenly disappear, and the Ar_2^+ ions become dominant, since their density drops more slightly (cf. the three small peaks at 0.8, 0.9 and 1.0 ms). This is the result of the fast ion conversion of Ar^+ to Ar_2^+ due to the process $Ar^+ + 2Ar \rightarrow Ar_2^+ + Ar$. This also explains why the electron density exhibits a shade in the post-discharge, as it is related to the evolution of the Ar_2^+ ion density (see details below). The low charged particle density is important when using the post-discharge for surface treatment, as it will suppress damage effects due to ion bombardment and prevent surface modification by ion impact [43, 44].

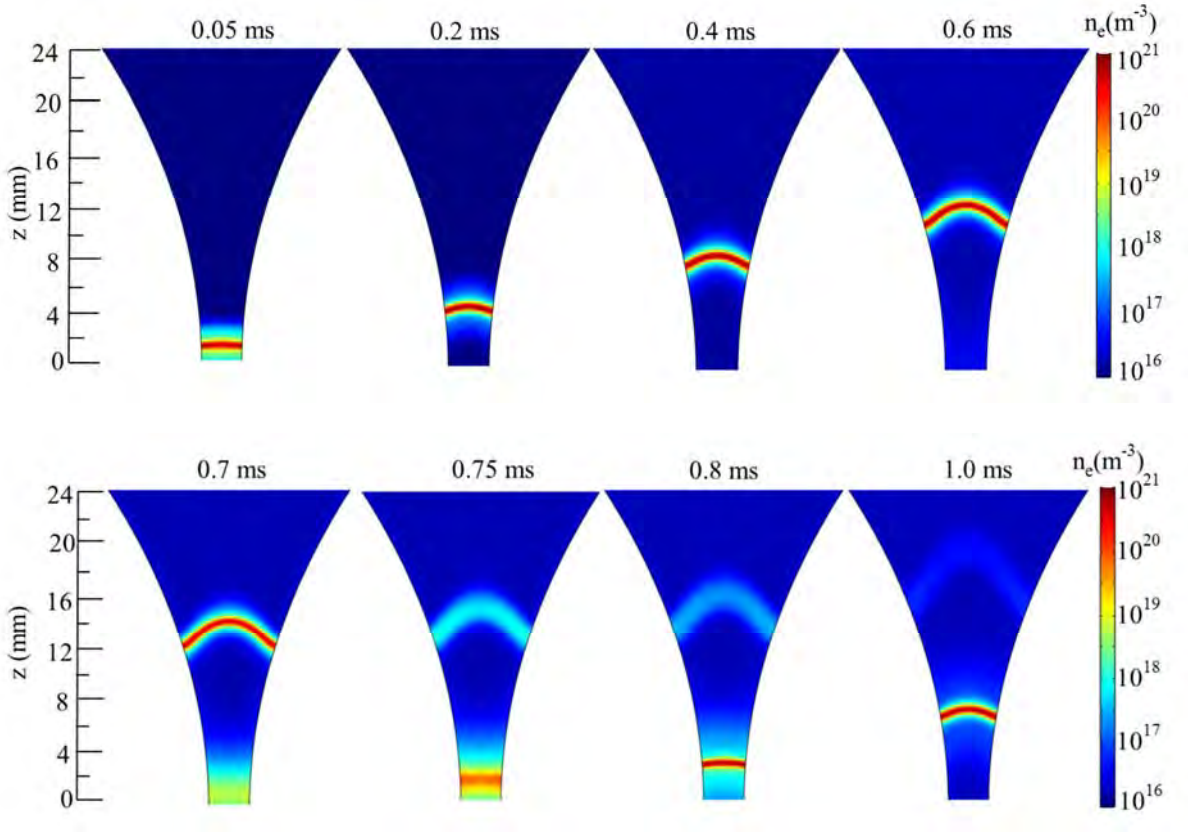

Figure 8. Time and spatial evolution of the electron density in the yz plane, at a current of 28 mA and a gas flow rate of 10 L/min.

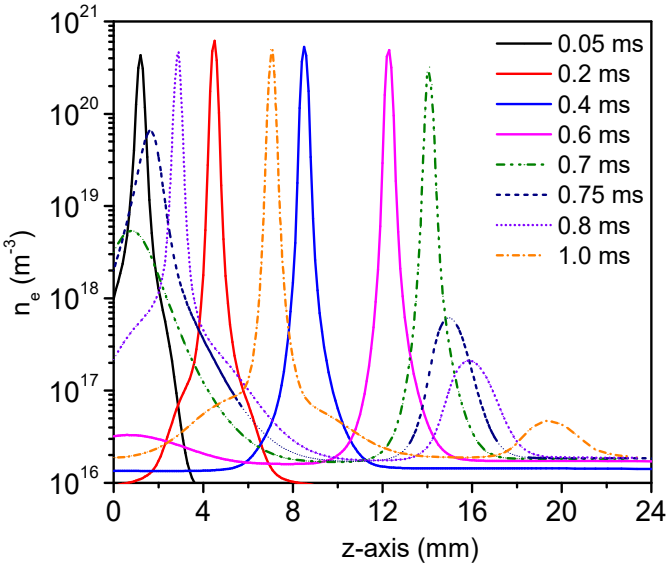

Figure 9. Distribution of electron density along the z-axis at different times, for a current of 28 mA and a gas flow rate of 10 L/min.

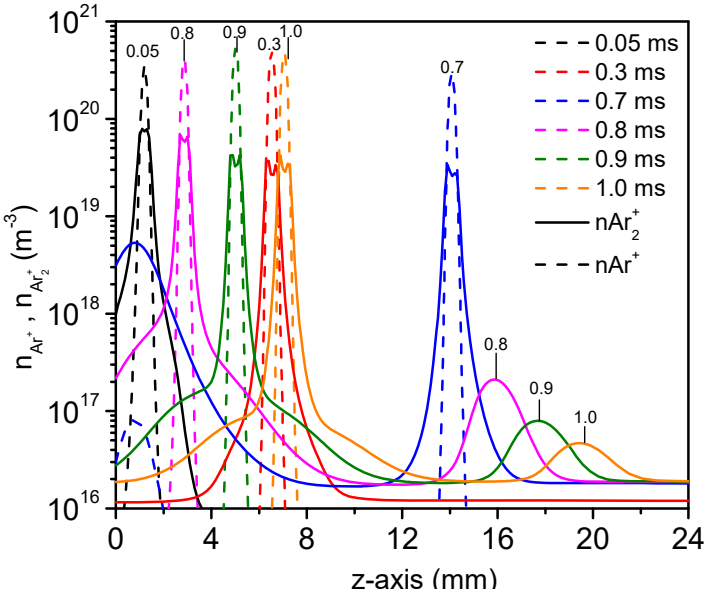

Figure 10. Distribution of Ar^+ (dashed lines) and Ar_2^+ (solid lines) ion density along the z-axis at different times, for a current of 28 mA and a gas flow rate of 10 L/min.

The time and spatial evolution of the Ar_2^+ ion density is presented in figure 11. At the time of 0.05 ms, the density is quite high, i.e., about 7.5×10^{19} m^{-3}, i.e., only a factor 5.7 lower than the electron density (about 4.3×10^{20} m^{-3}, cf. figure 8), and a factor 4.7 lower than the Ar^+ density (about 3.55×10^{20} m^{-3}, cf. figure 10). This is due to the low gas temperature at this moment (see explanation below). With increasing time, the Ar_2^+ ions have a somewhat higher density at the borders of the arc, while in the arc core zone, their density is lower. This is different from the electron density distribution and the Ar^+ ion density distribution (not shown), which exhibit their maximum in the core of the arc. This behavior can be explained from the gas temperature distribution, because at a low gas temperature, the Ar^+ ions are converted into Ar_2^+ ions by the three-body conversion reaction ($Ar^+ + 2Ar \rightarrow Ar_2^+ + Ar$). From the time and spatial evolution of the gas temperature in figure 6, it can be clearly seen that the gas temperature gradually decreases away from the arc core zone, resulting in a higher Ar_2^+ ion density at the arc borders.

When the old arc decays, i.e., in the post-discharge stage, there is a clear shade in the Ar_2^+ density profile at the time of 0.75 ms, in the order of 6×10^{17} m^{-3}. This distribution is the same as the distribution of electron density in the post-discharge stage (cf. figure 8 above), while the Ar^+ ion density is already extremely low in this time interval (see figure 10), due to the fast ion conversion of Ar^+ to Ar_2^+, as explained above. Although the electron temperature and the reduced electric field are very low in the post-discharge, the charged particle densities gradually decrease as a result of diffusion and recombination. The major recombination process which take place in the post-discharge plasma is $Ar_2^+ + e \rightarrow Ar + Ar(4s)$, while in the active arc phase the recombination processes are dominated by $Ar_2^+ + e \rightarrow Ar + Ar(4s)$ and $Ar^+ + e + Ar \rightarrow Ar + Ar$.

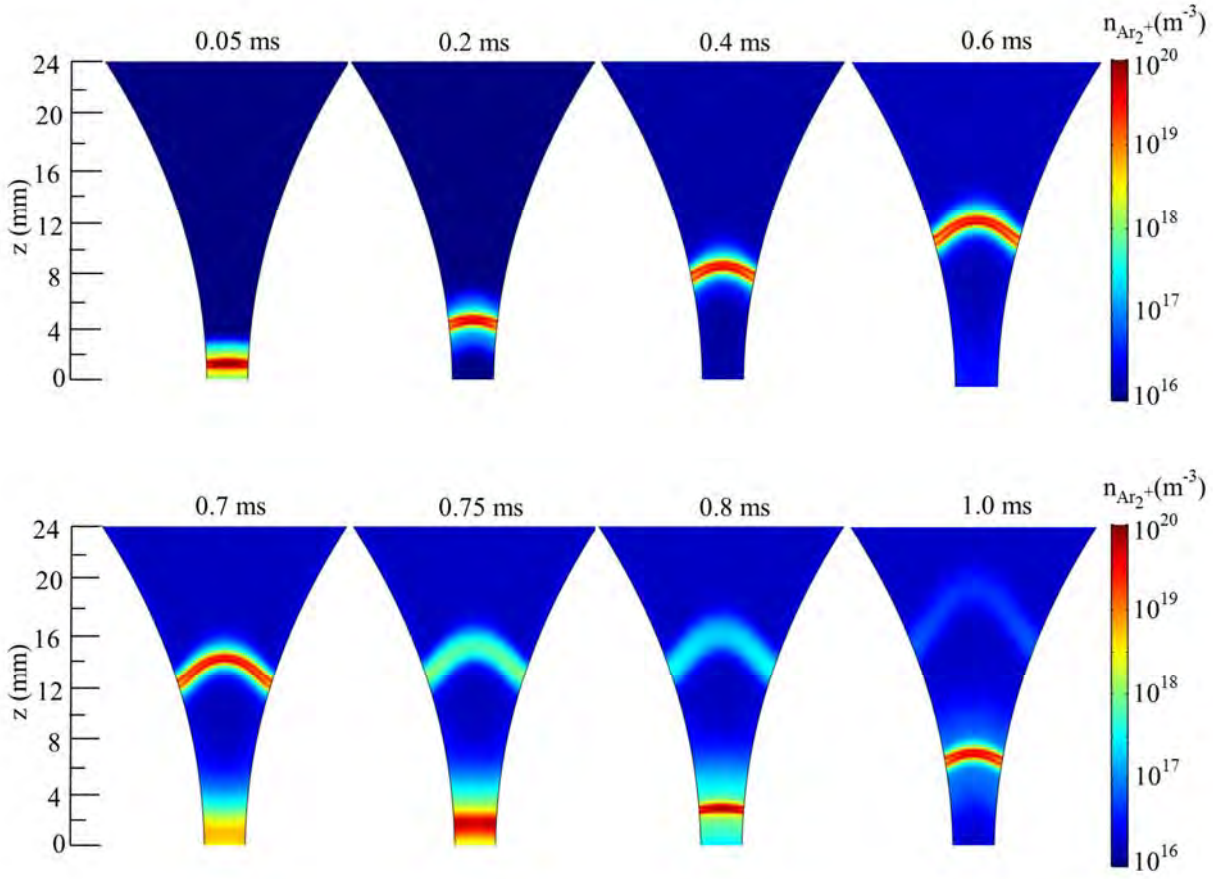

Figure 11. Time and spatial evolution of the Ar_2^+ ion density in the yz plane, at a current of 28 mA and a gas flow rate of 10 L/min.

Finally, the time and spatial evolution of the Ar(4s) excited state density is presented in figure 12. At the time of 0.05 ms, the Ar(4s) density is very high, i.e., 9×10^{19} m^{-3}, due to the high electron temperature at this moment. After ignition of the arc, the Ar(4s) density slightly decreases during the arc downstream movement. At the time of 0.7 ms, the density at the shortest gap increases again due to the appearance of a new arc and the repetition of the arc cycle.

In the post-discharge plasma at time 0.75 ms, the Ar(4s) density in the first arc has dropped to about 5×10^{16} m^{-3}, but the plasma column is again wider compared to the active arc. Later, the density decreases further to negligible values. Therefore, when using the post-discharge for surface treatment, it is important to ensure that the excited states reach the target object rapidly, before their density decays, resulting in slow reactions.

Overall, from the results presented above, we can conclude that the species densities and the electron temperature reach more or less constant values very quickly after the arc ignition. For gas treatment this could give a clue for more optimal conditions. Indeed, if the reactions of interest leading to certain gas conversion are fast (much faster than the gliding arc cycle, which is several ms in reality) and thus a chemical equilibrium is reached, one does not need to sustain the discharge for a longer time in the order of milliseconds but it might be more interesting to use pulsing with shorter period in the order of tens of microseconds. This is also

valid with respect to surface treatment using the post-discharge plasma: the excited species are formed in a short time, which suggests that the exposure time to the discharge stage might be drastically shortened, even down to a series of short pulses [45].

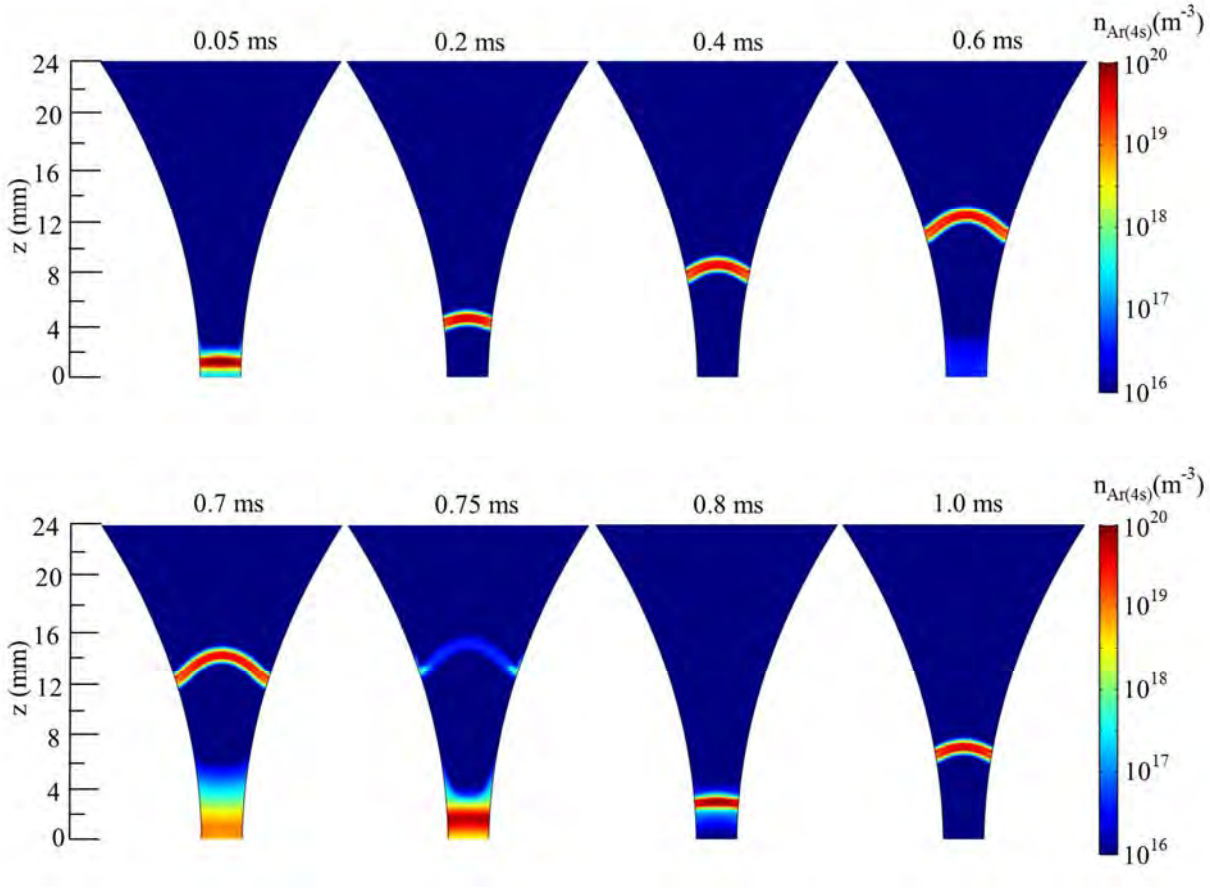

Figure 12. Time and spatial evolution of the Ar(4s) excited state density in the yz plane, at a current of 28 mA and a gas flow rate of 10 L/min.

4. Conclusions

We have investigated in detail the plasma discharge and post-discharge characteristics of a gliding arc in argon by means of a 3D model. The calculated gas temperature is compared with experimental values to validate our model, and the agreement is quite reasonable, certainly when compared to previous 2D model calculations, where much higher gas temperatures were predicted due to the absence of turbulent convective cooling. Also our calculated electron density is in reasonable agreement with experimental data from literature. Therefore, we believe that our 3D model can quantitatively reproduce the real gliding arc behavior.

In the plasma discharge stage, the electron temperature and reduced electric field are high to sustain the arc. This results in a high density of charged and excited species, allowing the discharge zone to be used for gas treatment, i.e., using the high energy electrons to react with the gas, giving rise to excitation, dissociation and ionization. However, in the post-discharge

stage, the electron temperature and reduced electric field drop over a very short time, and the densities of charged and excited species are relatively low.

In some applications, such as plasma sterilization [46-48], the neutral species with considerable internal energy play a major role. They could reach the target as part of the post-discharge plasma, but our results indicate that their densities also drop rather quickly as a function of time in the post-discharge. Hence, both the direct exposure to the plasma discharge and post-discharge have specific limitations. Our detailed investigation of the plasma characteristics in the discharge and post-discharge of the gliding arc allows to select the most appropriate discharge stage, according to the practical needs. When a high energy and high densities of charged particles are needed, it is better to use the active discharge stage, but the latter is accompanied with a high gas temperature. If a low gas temperature is needed, and the neutral species are important for the application, the post-discharge is more appropriate, but our results indicate that the densities of all species drop quickly. Finally, it is clear from our results that the gliding arc combines the discharge and post-discharge together and periodically produces both types of plasmas.

Acknowledgments

This work is financially supported by the Methusalem financing, by the Fund for Scientific Research Flanders (FWO) and by the IAP/7 (Inter-university Attraction Pole) program "Physical Chemistry of Plasma-Surface Interactions" from the Belgian Federal Office for Science Policy (BELSPO). The work was carried out in part using the Turing HPC infrastructure of the CalcUA core facility of the Universiteit Antwerpen, a division of the Flemish Supercomputer Center VSC, funded by the Hercules Foundation, the Flemish Government (department EWI) and the Universiteit Antwerpen. This work was also supported by the National Natural Science Foundation of China. (Grant Nos. 11275021, 11575019). SR Sun thanks the financial support from the China Scholarship Council (CSC).

References

[1] Kusano Y, Sorensen B F, Andersen T L and Leipold F 2013 Adhesion Improvement of glass-fibre-reinforced polyester composites by gliding arc discharge treatment J. Adhes. 89: 433–59
[2] Lee H, Sekiguchi H 2011 Plasma–catalytic hybrid system using spouted bed with a gliding arc discharge: CH_4 reforming as a model reaction J. Phys. D: Appl. Phys. 44: 274008 (8pp)
[3] Kalra C S, Gutsol A F and Fridman A A 2005 Gliding arc discharges as a source of intermediate plasma for methane partial oxidation IEEE Trans. Plasma Sci. 33 32–41
[4] Indarto A, Choi J W, Lee H and Song H K, 2006, Conversion of CO_2 by Gliding Arc Plasma Environmental Engineering Science 23(6): 1033-1043
[5] Fridman A, Nester S, Kennedy L A, Saveliev A and Mutaf-Yardimci O, 1999 Gliding arc gas discharge Progress in energy and combustion science 25: 211-231
[6] Korolev Y D, Frants O B, Geyman V G, Landl N V, and Kasyanov V S 2011 Low-Current “Gliding Arc” in an Air Flow IEEE Trans. Plasma Sci. 39(12) 3319–3325
[7] Pellerin S, Richard F, Chapelle J, Cormier J-M and Musiol K 2000 Heat string model of bi-dimensional dc Glidarc J. Phys. D: Appl. Phys. 33 2407–19

[8] Czernichowski A, 1994 Gliding arc. Applications to engineering and environment control Pure & Appl. Chem., 66(6): 1301-1310
[9] Kusano Y, Norrman K, Drews J et al., 2011 Gliding arc surface treatment of glass-fiber-reinforced polyester enhanced by ultrasonic irradiation Surface & Coatings Technology 205: S490-S494.
[10] Benstaali B, Moussa D, Addou A, Brisset J L. 1998 Plasma treatment of aqueous solutes: some chemical properties of a gliding arc in humid air. Eur. Phys. J. AP 4: 171–179.
[11] Mountapmbeme-Kouotou P , Laminsi S , Acayanka E , Brisset J L 2013 Degradation of palm oil refinery wastewaters by non-thermal gliding arc discharge at atmospheric pressure Environmental Monitoring and Assessment, 185(7): 5789–5800
[12] Moussa D, Abdelmalek F, Benstaali B, Addou A, Hnatiuc E, Brisset J L 2005 Acidity control of the gliding arc treatments of aqueous solutions: application to pollutant abatement and biodecontamination. Eur Phys J Appl Phys, 29:189–99
[13] Abdelmalek F, Guarbi S, Benstaali B, Addou A, Brisset J L 2004 Plasma chemical degradation of azo dyes by humid air plasma: yellow supranol 4 GL, scarlet red nylosan F3 GL and industrial waste. Water Res 38: 2338–46.
[14] Vitrac H, Guespin-Michel J, Brisset J L 2000 A microbiological investigation of the gliding arc treatment of aqueous media. In the proceedings of the International Symposium on High Pressure, Low Temperature Plasma Chemistry, Hakone VII, Greifswald, Germany; p. 393–7.
[15] Merouani D R, Abdelmalek F, Ghezzar M R, Semmoud A, Addou A, and Brisset J L 2013 Influence of Peroxynitrite in Gliding Arc Discharge Treatment of Alizarin Red S and Postdischarge Effects Ind. Eng. Chem. Res. 52: 1471−1480.
[16] Moussa D, Doubla A, Kamgang-Youbi G, and Brisset J L 2007 Postdischarge Long Life Reactive Intermediates Involved in the Plasma Chemical Degradation of an Azoic Dye IEEE Trans. Plasma Sci. 35(2) 444–453
[17] Bo Z, Yan J, Li X, Chi Y and Cen K, 2008 Plasma assisted dry methane reforming using gliding arc gas discharge: Effect of feed gases proportion Int. J. Hydrogen Energy, 33(20): 5545-5553.
[18] Toshifuji J , Katsumata T, Takikawa H, Sakakibara T, Shimizu I 2003 Cold arc-plasma jet under atmospheric pressure for surface modification Surface and Coatings Technology 171: 302–306
[19] Kolev St, Bogaerts A, 2015 A 2D model for a gliding arc discharge Plasma Sources Sci. Technol. 24 015025.
[20] Kolev St, Bogaerts A, 2015 Similarities and differences between gliding glow and gliding arc discharges Plasma Sources Sci. Technol. 24 065023
[21] Sun S, Kolev St, Wang H X and Bogaerts A, 2017 Coupled gas flow-plasma model for a gliding arc: investigations of the back-breakdown phenomenon and its effect on the gliding arc characteristics Plasma Sources Sci. Technol. 26 015003
[22] Freton P, Gonzalez J J and Gleizes A 2000 Comparison between a two- and a three dimensional arc plasma configuration J. Phys. D: Appl. Phys. 33: 2442–2452
[23] Gonzalez J J, Lago F, Freton P, Masquere M and Franceries X 2005 Numerical modeling of an electric arc and its interaction with the anode: part II. The three-dimensional model—influence of external forces on the arc column J. Phys. D: Appl. Phys. 38: 306–318
[24] Gonzalez J J, Freton P and Gleizes A 2002 Comparisons between two- and three-dimensional models: gas injection and arc attachment J. Phys. D: Appl. Phys. 35: 3181–3191
[25] Trelles J P, Pfender E, Heberlein J V R 2006 Multiscale Finite Element Modeling of Arc Dynamics in a DC Plasma Torch Plasma Chem Plasma Process 26: 557–575
[26] Trelles J P, Pfender E and Heberlein J V R 2007 Modelling of the arc reattachment process in plasma torches J. Phys. D: Appl. Phys. 40: 5635–5648

[27] Trelles J P, Heberlein J V R and Pfender E 2007 Non-equilibrium modelling of arc plasma torches J. Phys. D: Appl. Phys. 40 5937–5952
[28] Trenchev G, Kolev St and Bogaerts A 2016 A 3D model of a reverse vortex flow gliding arc reactor Plasma Sources Sci. Technol. 25 035014
[29] Zhu J, Sun Z, Li Z, Ehn A, Alden M, Salewski M, Leipold F and Kusano Y 2014 Dynamics, OH distributions and UV emission of a gliding arc at various flow-rates investigated by optical measurements J. Phys. D: Appl. Phys. 47 295203 (11pp)
[30] Kolev S, Sun S R, Trenchev G, Wang W Z, Wang H X, Bogaerts A 2016 Quasi-neutral modeling of gliding arc plasmas plasma processes and polymers DOI: 10.1002/ppap.201600110
[31] Tu X, Gallon H J, Whitehead J C 2011 Electrical and optical diagnostics of atmospheric pressure argon gliding arc plasma jet 30th ICPIG (Belfast, UK, 28 August– 2 September, 2011) C10
[32] Tu X, Gallon H J and Whitehead J C, 2011 Dynamic Behavior of an Atmospheric Argon Gliding Arc Plasma IEEE Trans. Plasma Sci. 39(11): 2900–1.
[33] Wilcox D C, 1988 Reassessment of the Scale-Determining Equation for Advanced Turbulence Models, AIAA Journal, 26(11): 1299-1310.
[34] Bartosiewicz Y, Proulx P and Mercadier Y 2002 A self-consistent two-temperature model for the computation of supersonic argon plasma jets J. Phys. D: Appl. Phys. 35: 2139–2148.
[35] Beulens J J, Milojevic D, Schram D C, and Vallinga P M 1991 A two-dimensional nonequilibrium model of cascaded arc plasma flows Physics of Fluids B: Plasma Physics 3: 2548-2557.
[36] Baeva M, Benilov M S, Almeida N A and Uhrlandt D 2016 Novel non-equilibrium modelling of a DC electric arc in argon J. Phys. D: Appl. Phys. 49: 245205.
[37] Tu X, Chéron B G, Yan J H, Yu L, and Cen K F 2008 Characterization of an atmospheric double arc argon-nitrogen plasma source, Physics of plasmas, 15: 053504-1-10.
[38] Tu X, Cheron B G, Yan J H and Cen K F, 2007 Electrical and spectroscopic diagnostic of an atmospheric double arc argon plasma jet, Plasma Sources Sci. Technol. 16: 803–812.
[39] Wu A J, Zhang H, Li X D, Lu S Y, Du C M, and Yan J H 2015 Determination of Spectroscopic Temperatures and Electron Density in Rotating Gliding Arc Discharge, IEEE Transactions on plasma science, 43(3): 836-845.
[40] EI-Zein A, Talaat M, EI-Aragi G, EI-Amawy A 2015 Experimental Model to Study the Characteristics of Gliding Arc Plasma Reactor with Argon/Nitrogen, Journal of Electrical Engineering, 15: 64-67.
[41] Eliasson B, and Kogelschatz U 1991 Nonequilibrium Volume Plasma Chemical Processing, IEEE Transactions on plasma science, 19 (6): 1063-1077.
[42] Zhu J, Gao J, Li Z, Ehn A, Aldén M, Larsson A, and Kusano Y, 2014 Sustained diffusive alternating current gliding arc discharge in atmospheric pressure air, Applied Physics Letters, 105: 234102
[43] Belmonte T, Czerwiec T, Michel H 2001 Fundamentals and applications of late post discharge processes *Surface and Coatings Technology* 142-144: 306-313.
[44] Moreau S, Moisan M, Tabrizian M, Barbeau J, Pelletier J, Ricard A, and Yahia L H 2000 Using the flowing afterglow of a plasma to inactivate Bacillus subtilis spores: Influence of the operating conditions *Journal of Applied Physics* 88(2) 1166-1174.
[45] Brisset J L, Moussa D, Doubla A, Hnatiuc E, Hnatiuc B, Youbi G K, Herry J M, Naïtali M, and Bellon-Fontaine M N 2008 Chemical Reactivity of Discharges and Temporal Post Discharges in Plasma Treatment of Aqueous Media: Examples of Gliding Discharge Treated Solutions *Ind. Eng. Chem. Res.* 47: 5761–5781.

[46] Moisan M, Barbeau J, Moreau S, Pelletier J, Tabrizian M, Yahia L H 2001 Low temperature sterilization using gas plasmas: a review of the experiments and an analysis of the inactivation mechanisms *International Journal of Pharmaceutics* 226: 1 – 21.
[47] Pintassilgo C D, Kutasi K and Loureiro J 2007 Modelling of a low-pressure N_2–O_2 discharge and post-discharge reactor for plasma sterilization Plasma Sources Sci. Technol. 16: S115–S122.
[48] Villeger S, Cousty S, Ricard A and Sixou M 2003 Sterilization of E. coli bacterium in a flowing N_2–O_2 post-discharge reactor J. Phys. D: Appl. Phys. 36: L60–L62.